nature methods

Brief Communication

https://doi.org/10.1038/s41592-023-02030-7

Molecular mechanocytometry using tension-activated cell tagging

Received: 20 May 2022

Accepted: 22 August 2023

Published online: 05 October 2023

Check for updates

Rong Ma[1], Sk Aysha Rashid[1,4], Arventh Velusamy[1,4], Brendan R. Deal[1,4], Wenchun Chen[2], Brian Petrich[2], Renhao Li[2] & Khalid Salaita[1,3]

Flow cytometry is used routinely to measure single-cell gene expression by staining cells with fluorescent antibodies and nucleic acids. Here, we present tension-activated cell tagging (TaCT) to label cells fluorescently based on the magnitude of molecular force transmitted through cell adhesion receptors. As a proof-of-concept, we analyzed fibroblasts and mouse platelets after TaCT using conventional flow cytometry.

Using antibodies and complementary nucleic acids to label cells fluorescently followed by analysis using flow cytometry and fluorescence-activated cell sorting (FACS) is a cornerstone of modern biological sciences. It would be highly desirable to also measure the mechanical profile of single cells using flow cytometry as this offers a complementary biophysical marker to chemical markers[1–3]. Accordingly, a suite of flow cytometry methods has been developed to readout cell mechanics by measuring cell deformation during hydrodynamic stretching or microconstriction[4–6]. For example, in real-time deformability cytometry, a high-speed camera records the transient deformation of cells while passing through a narrow channel under shear flow[7]. Deformation-based cytometry methods are powerful and have demonstrated clinical potential by detecting disease-specific changes in the mechanical deformation of cells[8,9]. One challenge for deformability measurements is these are a convoluted product of several parameters that include cell volume, membrane composition, cytoskeletal dynamics and cell cycle[10–13]. Thus, there is a need to develop mechanophenotyping platforms that employ molecular markers of mechanotransduction. To date, the readout of molecular forces generated by cells is performed using high-resolution fluorescence microscopy, which is low throughput[14–17]. Indeed, there are no flow cytometry or FACS-like techniques that can tag/sort cells based on the magnitude of molecular forces generated (Supplementary Table 1)[18,19].

To address this gap, we have developed TaCT (Fig. 1a), which enables flow cytometry-based identification and sorting of mechanically active cells based on the molecular forces transmitted by their surface adhesion receptors. TaCT probes are engineered DNA duplexes that have a digital response to a pN force and release a cholesterol-modified strand that spontaneously incorporates into the membrane of force-generating cells.

TaCT takes advantage of the fundamental mechanism of double-stranded (ds) DNA 'peeling' under force[20]. When a short DNA duplex is stretched from both ends of one of the strands (3′–5′ pulling; Fig. 1b(i)), the duplex is destabilized and can denature (peeling; Fig. 1b(ii)), leading to complementary DNA separation (separation; Fig. 1b(iii))[20–22]. Due to the narrow range of forces at which the denaturation transition occurs (Fig. 1b and Supplementary Fig. 1), it can be characterized as a simple two-state system, that is, we can treat the DNA duplex as either being in dsDNA form or in completely separated single-stranded (ss) DNA form. For example, a 24-base oligonucleotide (24-mer) duplex (Supplementary Table 2) was reported to peel at a force $F = 41$ pN using magnetic tweezer measurements[20]. To confirm the critical peeling force for this 24-mer, we used the oxDNA coarse-grained model to apply a load of 2.81×10^3 nm s^{-1} and recorded the number of base pairs in the duplex[23]. The peeling force (F_{peel}) was defined as the force at which the number of base pairs in the duplex is less than or equal to five. We found that $F_{peel} = 41 \pm 2.8$ pN (mean ± s.d.) by averaging the first 100 datapoints in the simulation (Fig. 1b, Supplementary Video 1 and Supplementary Fig. 1).

The TaCT probe comprised a load-bearing strand and a 24-mer peeling strand. The load-bearing strand displayed the RGD integrin ligand at one terminus and was attached to the glass slide through its other terminus. The load-bearing strand also incorporated an internal Cy3B dye. The complementary peeling strand was designed to release once $F > F_{peel}$ and its termini were labeled with Atto647N and cholesterol (Fig. 1a and Supplementary Fig. 2). TaCT probes were annealed and immobilized on streptavidin-coated glass slides (Supplementary Fig. 3). At rest, the probe is duplexed and Cy3B and Atto647N form a Förster resonance energy transfer (FRET) pair. When $F > F_{peel}$, the Atto647N strand peels and dissociates, while the Cy3B dye on the load-bearing strand is dequenched. The FRET efficiency for TaCT

[1]Department of Chemistry, Emory University, Atlanta, GA, USA. [2]Department of Pediatrics, Emory University, Atlanta, GA, USA. [3]Wallace H. Coulter Department of Biomedical Engineering, Emory University and Georgia Institute of Technology, Atlanta, GA, USA. [4]These authors contributed equally: Sk Aysha Rashid, Arventh Velusamy, Brendan R. Deal. e-mail: k.salaita@emory.edu

https://doi.org/10.1038/s41592-023-02030-7

probes was 93.8% and hence the Cy3B signal is enhanced by more than tenfold upon peeling (Supplementary Fig. 4a). The probe density was measured at 5,200 ± 286 molecules μm^{-2}, which then allowed us to convert the Cy3B fluorescence signal to percentage peel (%peel) (Supplementary Fig. 4b,c)[24,25].

To demonstrate that cell-generated forces drive DNA duplex peeling, mouse embryonic fibroblasts (MEF) were plated on TaCT probe surfaces and then imaged using conventional fluorescence microscopy (Fig. 1c and Supplementary Video 2). A time-lapse video showed cell spreading that coincided with Cy3B signal, confirming integrin binding to RGD on TaCT probes. The Cy3B signal was localized primarily to the cell edge, consistent with the distribution of focal adhesions (FAs), and accumulated over time (Fig. 1d). The growth of Cy3B signal corresponded to the loss of Atto647N signal, confirming force-induced peeling (Fig. 1e). This mechanism can generate high quality maps of integrin forces independent of cholesterol conjugation to the probe (Extended Data Fig. 1a and Supplementary Fig. 5). Quantitative microscopy analysis of 227 cells showed that 0.9 ± 0.3% of probes peeled under each cell, equivalent to 47 ± 16 mechanical events μm^{-2} with $F > 41$ pN (Extended Data Fig. 1b). The observed tension signal colocalized with markers of FAs such as vinculin and phosphorylated FA kinase (FAK pY397), as well as actin stress fibers (Extended Data Fig. 1c–e), confirming that forces were transmitted primarily by integrins within FAs[26]. Importantly, the peeling signal mirrors that of the turn-on tension gauge tether (TGT) probes (Extended Data Fig. 2a,b) but avoids the termination of mechanotransduction, which represents a great advantage as a molecular force sensor (Extended Data Fig. 2a,c,d and Supplementary Note). Control groups of cells treated with Latrunculin B (Lat B), which inhibits actin polymerization and disrupts force generation, showed substantial reduced peeling signal, as expected (Extended Data Fig. 3a,b). Cells treated with Lat B 50 min after seeding did not show tension signal changes, validating that the peeling mechanism is irreversible, producing maps of accumulated mechanical events over time. As expected, addition of soluble peeling strand (with BHQ2) led to the loss of the tension signal in cells treated with Lat B, showing a simple approach to resetting tension signal and recording real-time events (Extended Data Fig. 3c–f).

After confirming that DNA peeling faithfully maps molecular traction forces, we next investigated cholesterol–DNA cell tagging for TaCT (Fig. 1a). Previous work showed that cholesterol–DNA can partition into the plasma membrane of cells[27,28]. We discovered that cholesterol–ssDNA conjugates are ~50-fold more effective at tagging cells compared with cholesterol–dsDNA conjugates (Extended Data Fig. 4a,b and Supplementary Fig. 6). This is advantageous as it enhances the specificity of TaCT. We also verified that cholesterol–ssDNA membrane association is linearly proportional to the soluble conjugate concentrations tested (Extended Data Fig. 4c,d)[28]. The stability of TaCT tags was examined by incubating cholesterol–ssDNA with cells, washing and measuring the loss of DNA as a function of time. We found that ~20–30% of the cholesterol-tethered DNA had dissociated after 90 min (Extended Data Fig. 4e,f). Accordingly, we chose to incubate the cells on the surface for 1 h, which allowed for FA formation and TaCT to proceed while limiting cholesterol dissociation.

As a proof-of-concept, NIH3T3 cells were seeded onto the TaCT substrates, allowed to spread and then collected by gentle scraping. TaCT signal was then measured by flow cytometry. Probes lacking RGD, probes lacking cholesterol as well as full TaCT probes but with cells treated with Lat B were used as negative controls. The resulting flow cytometry histograms showed a heterogeneous distribution of TaCT signal, matching the tension signal distributions observed with microscopy (Fig. 1f and Extended Data Fig. 1b). The cells on the TaCT substrate showed 27.6 ± 4.0% force-positive population compared with 0.6 ± 0.2%, 1.1 ± 0.5% and 3.5 ± 2.0% in (−) cholesterol, (−) RGD and (+) Lat B controls, respectively (Fig. 1f and Extended Data Fig. 5). The Atto647N geometric mean fluorescence intensity (gMFI) of cells incubated on TaCT showed a greater than twofold increase compared with controls, whereas the Cy3B gMFI did not change (Extended Data Fig. 5). Taken together, this result confirmed that TaCT is triggered by force transmission through the integrin-RGD complex, followed by cholesterol-mediated membrane incorporation. Background tagging of cells due to cell spreading and proximity to the surface leads to negligible TaCT signal (Extended Data Fig. 6).

Next, we tested whether this strategy works in primary cells. Platelets were chosen for this demonstration as mechanical forces play a crucial role in platelet activation, aggregation and clot retraction, which are necessary steps in coagulation[29]. When mouse platelets were seeded onto the TaCT surface for 30 min, we noted loss of Atto647N signal that was coupled with an increase in Cy3B. This confirms that platelet integrin force transmission was sufficient to mediate DNA peeling with $F > 41$ pN (Fig. 1g). The Atto647N depletion signal did not colocalize exclusively with the Cy3B turn-on signal, which may be due to the accumulation of cholesterol–DNA probes at the basal face of the cell membrane (Extended Data Fig. 7a,b). Nonetheless, the TaCT signal was measured by flow cytometry, which showed 13.3 ± 2% force-positive population (Fig. 1h and Extended Data Fig. 7c). Control experiments withholding the divalent cations Mg^{2+} or Ca^{2+} necessary for full integrin activation showed minimal TaCT signal and force-positive population. Likewise, withholding ADP agonist inhibited platelet forces generation and TaCT signal, consistent with literature precedent[29,30]. Finally, withholding ADP but adding Mn^{2+} led to cell spreading but without platelet activation and this control also showed weak TaCT signal. Together, these experiments demonstrate that TaCT specifically tags platelets based on integrin molecular traction forces.

To showcase that TaCT is an effective method to report cell receptor forces, we used a Rho-associated protein kinase inhibitor, Y27632, to disrupt force transmission through cytoskeleton and measure the dose-dependent response in MEF cells. Y27632 inhibits Rho-associated protein kinase by competing with ATP binding, and further results

Fig. 1 | Tension-activated cell tagging. a, Schematic showing TaCT assay. **b**, Plot of 24-mer dsDNA stability as a function of applied force generated using oxDNA simulation with a loading rate of 2.81×10^3 nm s^{-1} (light green): (i) 3′5′ pulling; (ii) peeling; (iii) separation. Dark green shows the exponential moving average and indicates a 41 pN dehybridization transition. **c**, Time-lapse RICM and Cy3B fluorescence images of NIH3T3 cell spreading on TaCT surface at time t = 15–45 min after seeding. Scale bar, 10 µm. **d**, Line scan of Cy3B images noted by the yellow dashed line in **c**. ROI, region of interest. **e**, Representative RICM, Cy3B and Atto647N microscopy images of NIH3T3 cell cultured on TaCT substrate. Intensity bar for Cy3B image indicates the percentage of TaCT probes that undergo force-triggered release, whereas the intensity bar for Atto647N shows the signal normalized to the background of intact TaCT probes. Scale bar, 10 µm. Line scan shows anticolocalization of Cy3B and Atto647N intensities. **f**, Flow cytometry histograms of NIH3T3 cells cultured on TaCT substrates as well as control surfaces with (−) cholesterol, (−) RGD and (+) Lat B. Plot displays the force-positive population from $n \geq 3$ biological replicates (mean ± s.d., two-tailed Student's t-test). Gray dashed line indicates the gate for determining force-positive population. **g**, Representative RICM, Cy3B and Atto647N microscopy images of mouse platelets on TaCT substrates. Scale bar, 5 µm. **h**, Representative flow cytometry histograms of mouse platelets incubated on TaCT substrates. Gray dashed line indicates the gate for determining force-positive population. Controls included experiments with TaCT probes −RGD (gray), −divalent cations −ADP agonist (green), −ADP agonist (orange) and −ADP/+Mn^{2+} (blue). Data plotted from n = 3 animals (mean ± s.d., two-tailed Student's t-test). **i**, Schematic showing Y27632 treatment decreases integrin forces. ROCK, Rho-associated protein kinase. **j**, Quantitative analysis of the integrated Cy3B signal per cell from microscopy images of MEF cells pretreated with 0, 0.05, 0.5, 5, 10, 25 and 50 µM of Y27632 and cultured on peeling probe substrate. Plot shows the result from n = 3 biological replicates (mean ± s.e.m.). a.u., arbitrary units. **k**, TaCT signal of cells pretreated with different concentration of Y27632. Plot shows the result from n = 2–4 biological replicates.

https://doi.org/10.1038/s41592-023-02030-7

in decreased myosin activity, destabilization of actin filaments and abolished stress fiber formation (Fig. 1l)[31]. With Y27632 pretreatment, MEF cells showed decreased Cy3B tension signal (Fig. 1j and Supplementary Fig. 7). TaCT signal measured by flow cytometry showed a clear dose-dependent curve (Fig. 1k) with a half maximal inhibitory concentration (IC_{50}) = 773 nM, agreeing well with microscopy measurements and literature reported IC_{50} values from hundreds of nM to low µM amounts[32].

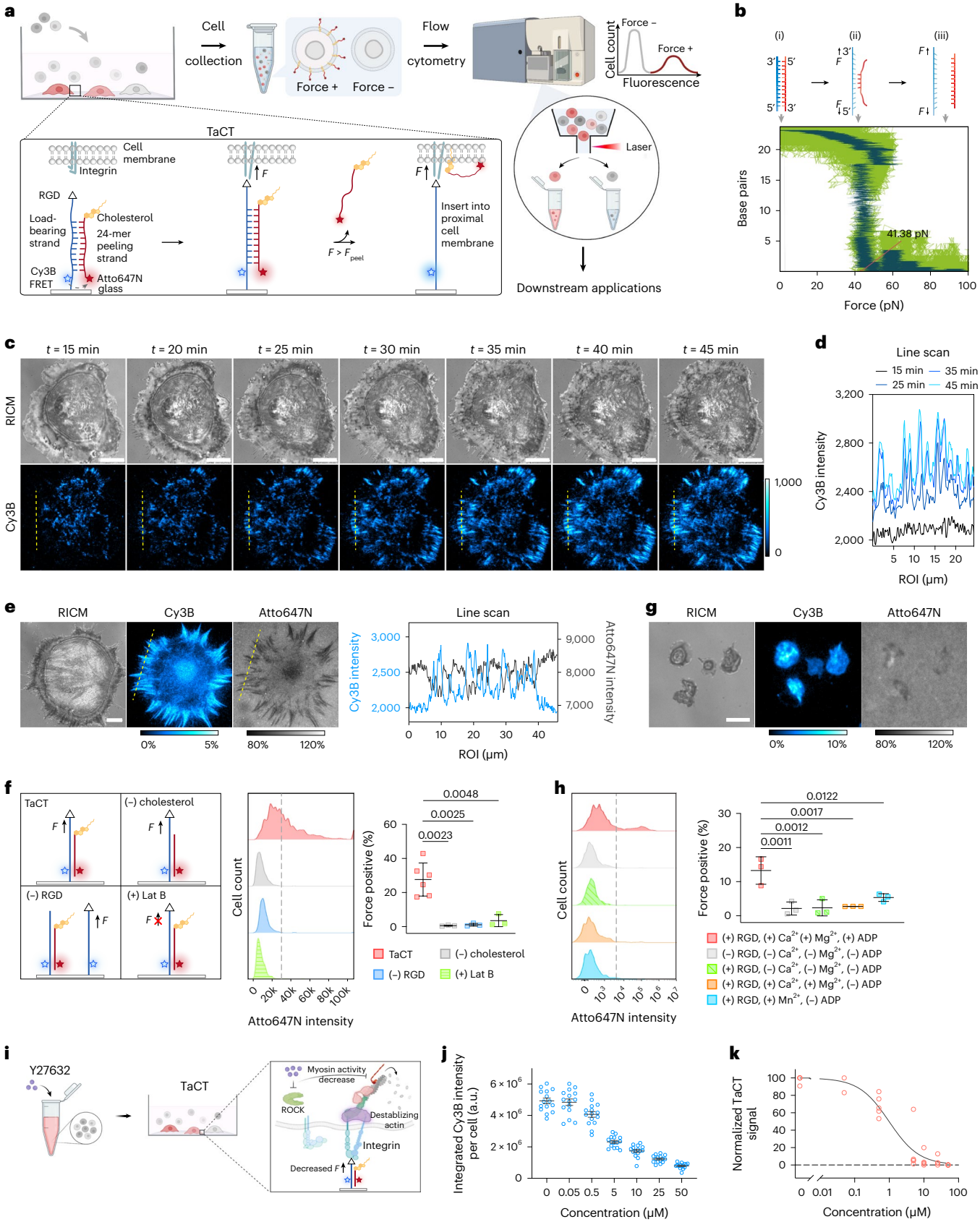

https://doi.org/10.1038/s41592-023-02030-7

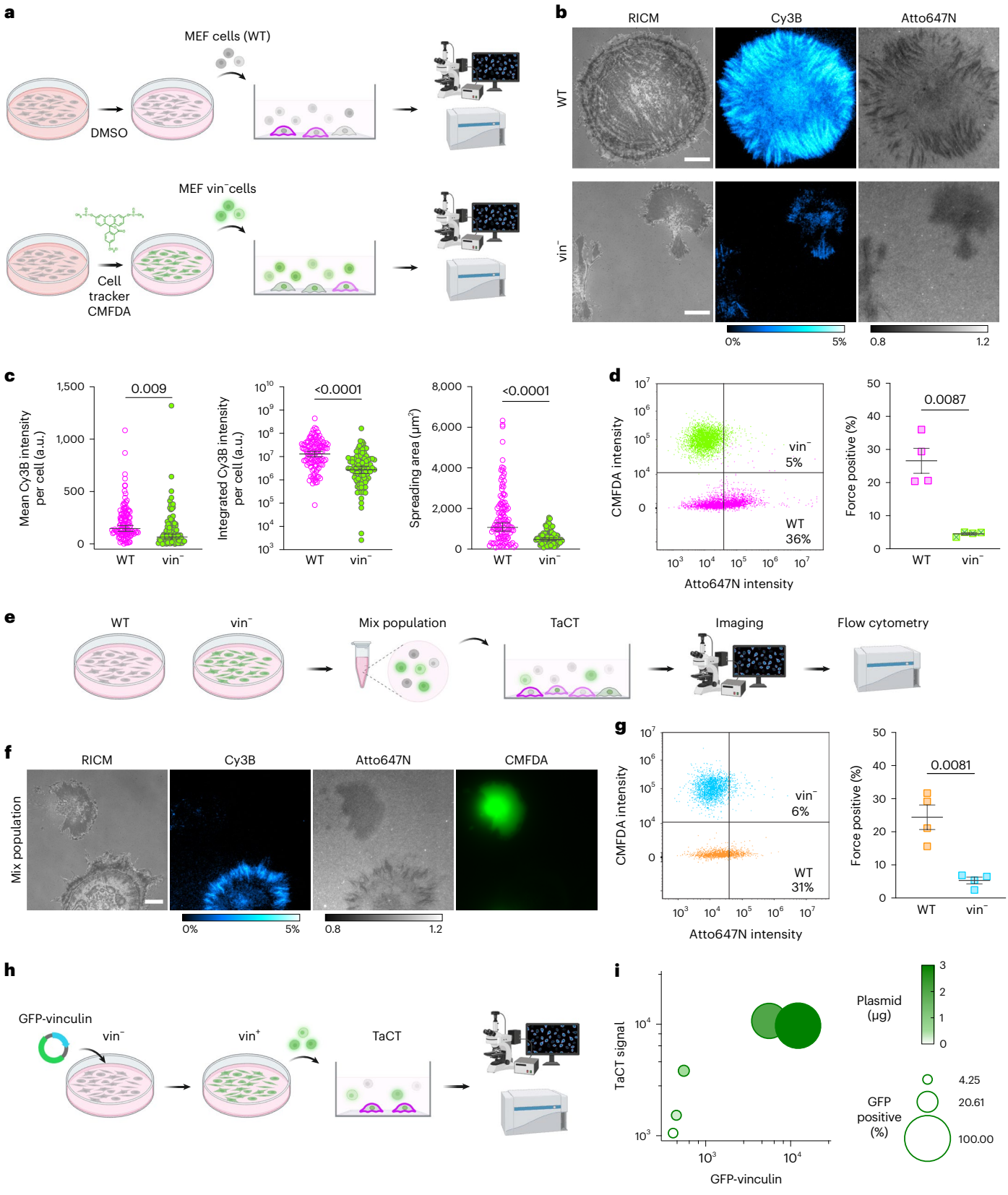

After demonstrating TaCT with a single population of cells, we sought to demonstrate analysis of a binary mixture of cells with differing mechanical activity. We used parental MEF cells (wild type (WT)) and MEF cells with vinculin null (vin⁻) for this demonstration. Vinculin is an adapter protein that localizes to FAs linking the cytoskeleton to adhesion receptors and aids in FA maturation (Extended Data Fig. 1a)[33]. We first performed TaCT on these two cell types separately. The vin⁻ cells were stained with cell tracker dye CMFDA before plating onto TaCT substrates (Fig. 2a). To ensure that the TaCT signal is not due to differential uptake, cholesterol uptake of WT and vin⁻ cells was measured by flow cytometry in parallel with each TaCT assay (Supplementary Fig. 8). As shown in Fig. 2b,c, WT cells had larger spreading area and

Fig. 2 | TaCT detecting mechanically active cells in a mixed population. **a**, Schematic showing TaCT workflow for MEF WT and vin$^-$ cells. MEF vin$^-$ cells were stained with CMFDA, and TaCT probe microscopy and flow cytometry analysis was performed ~1 h after cell seeding. **b**, Representative RICM, Cy3B and Atto647N microscopy images of WT and vin$^-$ cells seeded on TaCT substrates separately. Intensity bar for Cy3B image indicates the percentage of TaCT probes that undergo force-triggered release, and the intensity bar for Atto647N shows the signal normalized to the background. Scale bar, 10 µm. **c**, Plots showed that tension signal (Cy3B, mean and integrated) and spreading area of WT cells were significantly higher than in vin$^-$ cells (115 and 91 cells from $n = 3$ replicates, geometric mean ± 95% confidence interval, two-tailed Student's t-test). **d**, Representative flow cytometry density plot and quantification of force-positive cells show that WT cells had greater TaCT signal compared with vin$^-$ cells ($n = 4$ replicates, mean ± s.e.m., two-tailed paired Student's t-test). **e**, Schematic showing application of TaCT to cocultured WT/vin$^-$ cells. **f**, Representative RICM, Cy3B and Atto647N microscopy images of cocultured WT and vin$^-$ cells on TaCT substrate. Intensity bar for Cy3B image indicates the percentage of TaCT probes that undergo force-triggered release and the intensity bar for Atto647N shows the signal normalized to the background. Note that negative Atto647N signal for vin$^-$ cells was due primarily to cell–surface contact, which alters the local index of refraction. **g**, Representative flow cytometry density plot and quantification of force-positive cells show that WT cells had significantly greater TaCT signal and force-positive subpopulation compared with vin$^-$ cells incubated on the same TaCT substrate ($n = 4$ replicates, mean ± s.e.m., two-tailed paired Student's t-test). **h**, Schematic describing TaCT experiments using MEF vin$^-$ cells transfected with different amounts of plasmid that encodes GFP-vinculin. **i**, Plot showing vinculin expression (x axis, GFP MFI) versus TaCT signal (y axis, Atto647N MFI) with different amounts of plasmid transfected ($n = 4$ replicates). Green represents the amount of the GFP-vinculin plasmid, the size of the bubble represents the percentage GFP positive subpopulation.

produced more tension signal compared with vin$^-$ cells in the Cy3B channel. Flow cytometry also showed that there was more Atto647N signal in WT compared with vin$^-$ (Fig. 2d and Supplementary Fig. 8) (WT, 26.6 ± 3.7%; vin$^-$ 4.5 ± 0.3%). We then tested whether this differential tension signal could be detected when the WT and vin$^-$ were cocultured (Fig. 2e). As expected, WT cells displayed more TaCT tension signal by microscopy compared with vin$^-$ cells despite both effectively spreading on the substrate (Fig. 2f). The WT TaCT signal decreased slightly when these cells were cocultured, with a 24.4 ± 3.7% force-positive population compared with 5.2 ± 1.0% for vin$^-$ in the mixed population (Fig. 2g). The minimal TaCT signal change observed for vin$^-$ cells in coculture indicated that TaCT tags remain associated with target cells within the experimental time window (Supplementary Fig. 8). Together, these results confirm that TaCT can distinguish mechanically active subpopulations in heterogeneous mixtures of cells. To further demonstrate that TaCT produces a gradual response rather than a binary signal, we transfected MEF vin$^-$ cells with different amount of plasmid encoding green fluorescent protein (GFP)-vinculin (Fig. 2h). We next investigated the relationship between vinculin expression and tension by quantifying GFP and Atto647 intensity at the single-cell level. As expected, both the GFP and TaCT signal increased with increasing amount of plasmid (Fig. 2i and Supplementary Fig. 9). Interestingly, the TaCT signal recovered with relatively low levels of GFP-vinculin, showing a linear regime followed by saturation of tension at increasing levels of vinculin, which indicates a complex relationship between integrin tension and vinculin expression (Fig. 2i).

In conclusion, we take advantage of 3′–5′ mediated DNA peeling to develop a new class of DNA tension probes to map the molecular forces generated by cells and to enable high-throughput flow-cytometry-based detection of mechanically active cells. As is the case for all DNA tension probes, the probability of mechanical dehybridization is loading rate dependent. Therefore, to fully realize the potential of TaCT, future investigations into the precise loading rate and force duration of mechanoreceptors is required, and this needs to be coupled with the development of TaCT probes with different lengths and percentage of GC. TaCT signal reports the total number of mechanical events exceeding F_{peel}, which is orthogonal to biochemical analysis using antibodies and nucleic acids. The limit of detection of TaCT is akin to any other flow cytometry assay and, depending on the instrumentation and staining procedures, is probably capable of detecting hundreds of probes per cell. If greater force magnitude detection is desired, duplexes with greater F_{peel} should be designed. In applications that use TaCT to characterize mechanically active cells, it is important to include a cholesterol strand uptake calibration to account for potential cholesterol insertion differences between different cell types. A negative control that is not mechanically active should also be included to account for background uptake of cholesterol strands. Taken together, TaCT will open up a new class of tools for mechanobiology potentially allowing single-cell mechanical phenotypes to be linked with other biochemical properties.

Online content

Any methods, additional references, Nature Portfolio reporting summaries, source data, extended data, supplementary information, acknowledgements, peer review information; details of author contributions and competing interests; and statements of data and code availability are available at https://doi.org/10.1038/s41592-023-02030-7.

References

1. Di Carlo, D. A mechanical biomarker of cell state in medicine. *J. Lab. Autom.* **17**, 32–42 (2012).
2. Torrino, S. & Bertero, T. Metabo-reciprocity in cell mechanics: feeling the demands/feeding the demand. *Trends Cell Biol.* **32**, 624–636 (2022).
3. Evers, T. M. J. et al. Reciprocal regulation of cellular mechanics and metabolism. *Nat. Metab.* **3**, 456–468 (2021).
4. Belotti, Y. et al. High-throughput, time-resolved mechanical phenotyping of prostate cancer cells. *Sci. Rep.* **9**, 5742 (2019).
5. Islam, M. et al. Microfluidic cell sorting by stiffness to examine heterogenic responses of cancer cells to chemotherapy. *Cell Death Dis.* **9**, 239 (2018).
6. Lee, K. C. M. et al. Toward deep biophysical cytometry: prospects and challenges. *Trends Biotechnol.* **39**, 1249–1262 (2021).
7. Otto, O. et al. Real-time deformability cytometry: on-the-fly cell mechanical phenotyping. *Nat. Methods* **12**, 199–202 (2015).
8. Kozminsky, M. & Sohn, L. L. The promise of single-cell mechanophenotyping for clinical applications. *Biomicrofluidics* **14**, 031301 (2020).
9. Tse, H. T. et al. Quantitative diagnosis of malignant pleural effusions by single-cell mechanophenotyping. *Sci. Transl. Med.* **5**, 212ra163 (2013).
10. Thery, M. & Bornens, M. Get round and stiff for mitosis. *HFSP J.* **2**, 65–71 (2008).
11. Fletcher, D. A. & Mullins, R. D. Cell mechanics and the cytoskeleton. *Nature* **463**, 485–492 (2010).
12. Sanyour, H. J. et al. Membrane cholesterol and substrate stiffness co-ordinate to induce the remodelling of the cytoskeleton and the alteration in the biomechanics of vascular smooth muscle cells. *Cardiovasc. Res.* **115**, 1369–1380 (2019).
13. Guo, M. et al. Cell volume change through water efflux impacts cell stiffness and stem cell fate. *Proc. Natl Acad. Sci. USA* **114**, E8618–E8627 (2017).
14. Stabley, D. et al. Visualizing mechanical tension across membrane receptors with a fluorescent sensor. *Nat. Methods*. https://doi.org/10.1038/nmeth.1747 (2011).

15. Brockman, J. M. Live-cell super-resolved PAINT imaging of piconewton cellular traction forces. *Nat. Methods*. https://doi.org/10.1038/s41592-020-0929-2 (2020).
16. Ma, R. et al. DNA probes that store mechanical information reveal transient piconewton forces applied by T cells, *Proc. Natl Acad. Sci. USA*. https://doi.org/10.1073/pnas.1904034116 (2019).
17. Brockman, J. M. et al. Mapping the 3D orientation of piconewton integrin traction forces. *Nat. Methods* https://doi.org/10.1038/nmeth.4536 (2018).
18. Hang, X. et al. High-throughput DNA tensioner platform for interrogating mechanical heterogeneity of single living cells. *Small* **18**, e2106196 (2022).
19. Pushkarsky, I. et al. Elastomeric sensor surfaces for high-throughput single-cell force cytometry. *Nat. Biomed. Eng.* **2**, 124–137 (2018).
20. Yang, Z. et al. The kinetics of force-dependent hybridization and strand-peeling of short DNA fragments. *Sci. China Phys. Mech.* **59**, 192 (2016).
21. Cocco, S. et al. Overstretching and force-driven strand separation of double-helix DNA. *Phys. Rev. E* **70**, 011910 (2004).
22. Zhang, X. et al. Two distinct overstretched DNA structures revealed by single-molecule thermodynamics measurements. *Proc. Natl Acad. Sci. USA* **109**, 8103–8108 (2012).
23. Snodin, B. E. et al. Introducing improved structural properties and salt dependence into a coarse-grained model of DNA. *J. Chem. Phys.* **142**, 234901 (2015).
24. Zhang, Y. et al. DNA-based digital tension probes reveal integrin forces during early cell adhesion. *Nat. Commun.* **5**, 5167 (2014).
25. Galush, W. J., Nye, J. A. & Groves, J. T. Quantitative fluorescence microscopy using supported lipid bilayer standards. *Biophys. J.* **95**, 2512–2519 (2008).
26. Martino, F. et al. Cellular mechanotransduction: from tension to function. *Front Physiol.* **9**, 824 (2018).
27. Arnott, P. M. et al. Dynamic interactions between lipid-tethered DNA and phospholipid membranes. *Langmuir* **34**, 15084–15092 (2018).
28. You, M. et al. DNA probes for monitoring dynamic and transient molecular encounters on live cell membranes. *Nat. Nanotechnol.* **12**, 453–459 (2017).
29. Zhang, Y. et al. Platelet integrins exhibit anisotropic mechanosensing and harness piconewton forces to mediate platelet aggregation. *Proc. Natl Acad. Sci. USA* **115**, 325–330 (2018).
30. Duan, Y. et al. Mechanically triggered hybridization chain reaction. *Angew. Chem. Int. Ed. Engl.* **60**, 19974–19981 (2021).
31. Ishizaki, T. et al. Pharmacological properties of Y-27632, a specific inhibitor of rho-associated kinases. *Mol. Pharmacol.* **57**, 976–983 (2000).
32. Uehata, M. et al. Calcium sensitization of smooth muscle mediated by a Rho-associated protein kinase in hypertension. *Nature* **389**, 990–994 (1997).
33. Austen, K. et al. Extracellular rigidity sensing by talin isoform-specific mechanical linkages. *Nat. Cell Biol.* **17**, 1597–1606 (2015).

Methods

This research complies with all relevant ethical regulations.

Simulation of DNA peeling

The dsDNA peeling was modeled with oxDNA by adding harmonic traps (effectively springs) to two terminal nucleotides of a DNA stand (Supplementary Fig. 1). Each trap was assigned with a stiffness constant of 11.42 pN nm^{-1}, and one of the traps was moved at a given rate (loading rate, 2.81×10^3 nm s^{-1}) with respect to the other fixed trap. The effective stiffness constant of the two traps in series can be calculated using:

$$1/k_{\text{eff}} = 1/k_1 + 1/k_2$$

where k_1 and k_1 are the stiffness constants of the two traps and k_{eff} is the effective stiffness constant. The k_{eff} of the system is calculated to be 5.71 pN nm^{-1}. The total displacement of the two terminal nucleotides from the respective trap centers is defined as net displacement. Force is then calculated by multiplying k_{eff} with net displacement projected along the force axis (z axis). This force is plotted against the net displacement with an exponential moving average of datapoints. The oxDNA model considers base pairs as broken when the pairing energy is less than 10% of that of a fully formed base pair. The critical force at which peeling occurs (F_{peel}) is defined here as the force at which the total number of base pairs falls to less than or equal to five. The first 100 datapoints were averaged (to reduce the stochasticity in simulation data) to obtain the value of F_{peel}. Modeling parameters were adopted from published literature and from examples available at https://dna.physics.ox.ac.uk (ref. 34).

Oligonucleotide preparation

Conjugation with dyes. The load-bearing strand was conjugated with Cy3B NHS on the internal amine, the 24-mer peeling strand was conjugated with Atto647N NHS on the 5′ amine, and the TGT bottom strands were conjugated with Cy3B (Supplementary Table 2). Briefly, an excess amount of NHS dye (50 µg) was dissolved in dimethylsulfoxide immediately before use and then reacted with 10 nmol amine oligonucleotide at room temperature for 1 h in 1× phosphate-buffered saline (PBS) containing 0.1 M $NaHCO_3$. The mixture after reaction was desalted with P2 gel and purified with a high performance liquid chromatograph (HPLC) coupled to an advanced oligonucleotide C18 column (Supplementary Fig. 2). The product was eluted in solvents A (0.1 M TEAA) and B (acetonitrile) with linear gradients of 10–35% solvent B over 25 min and 35–100% solvent B over 5 min at 0.5 ml min^{-1} flow rate, and dried in a Vacufuge overnight. The dried oligo-dye conjugate was reconstituted in water and the concentration was determined by its absorbance at 260 nm with Nanodrop.

Conjugation with cRGD. Maleimide-cRGDfk was used for conjugation with thiol oligonucleotide strand (load-bearing strand). Briefly, 5 nmol of thiol oligonucleotide was reduced in 200× molar excess TCEP at room temperature for 15 min, and the mixture was added to 0.5 mg (excess) of maleimide-cRGDfk in 1× PBS (pH 6.8) to react at room temperature for 1 h. The reaction mixture was then desalted with P2 gel and purified by a HPLC with advanced oligonucleotide column as described above.

For the alkyne oligonucleotide TGT top quencher strand, azide-RGD was first prepared and then conjugated to the oligonucleotide. Briefly, excess azide-NHS (~0.5 mg) was used to react with 100 µg cyclic (RGD)fk-PEG2-amine overnight at 4 °C. The product was purified with a HPLC coupled to a Grace C18 column for peptide purification. Product was eluted in solvents A (0.1% TFA in H_2O) and B (0.1% TFA in acetonitrile) with linear gradients of 10–40% solvent B over 30 min and 40–75% solvent B over 10 min at 1 ml min^{-1} flow rate. The purified product was dried in a Vacufuge overnight. Stock solutions of $CuSO_4$ (20 mM in water), THPTA (Tris(3-hybroxypropyltriazolyl methyl) amine) (50 mM in water) and sodium ascorbate (100 mM in water) were prepared. A final mixture of 100 µM azide-RGD, 50 µM of alkyne-DNA, 0.1 mM $CuSO_4$, 0.5 mM THPTA and 5 mM sodium ascorbate in 1× PBS was allowed to react at room temperature for 2 h. The product was purified by P2 gel, followed by a HPLC with an advanced oligonucleotide column as described above.

DNA substrate preparation

Amine glass slides. Glass slides (25 × 75 mm^2) were placed on a Wash-N-Dry rack, rinsed with water (18.2 MΩ ultrapure water), and sonicated in ethanol and water for 15 min each, followed by six rinses with water. Fresh piranha solution was made by mixing concentrated sulfuric acid and hydrogen peroxide (30%) at a 3:1 ratio (v:v) in a total volume of 200 ml and added to the slides for etching (caution: piranha solution is highly reactive and may explode if mixed with organic solvents). Next, the slides were rinsed again with copious amounts of water to remove the acid, and then rinsed in ethanol to remove water. Then, 200 ml of 3% APTES in ethanol was prepared and added to the glass slides at room temperature to react for 1 h for amine modification. After reaction, the glass slides were washed with copious amounts of ethanol and bake-dried in an oven (80 °C) for 20 min. The amine modified glass slides were stored at −20 °C until use.

Biotin substrate preparation. An amine modified glass slide was placed carefully on a Parafilm-lined Petri dish. Then, 1 ml of 4 mg ml^{-1} Biotin-NHS in dimethylsulfoxide was added to the slide and incubated overnight. On the second day, after washing with copious amounts of ethanol and then water several times, the glass slide was air-dried, and attached to an ibidi sticky-slide imaging chamber or a bottomless adhesive 96-well plate. The wells were passivated in 1% bovine serum albumin (BSA) in PBS for 10 min at room temperature and then washed with PBS. Streptavidin at 50 µg ml^{-1} in PBS was added to each well and incubated for 30 min at room temperature, and the excess was washed away with PBS. Meanwhile, TaCT/peeling probe (load-bearing strand:peeling strand, 1:1.5) was annealed at 50 nM by heating to 95 °C for 5 min and then gradually cooling down to 20 °C in 20 min. For TGT substrates, the BHQ2 top strand was annealed with Cy3B bottom strand (1.1:1 ratio) at 50 nM. Next, the probes were added to each streptavidin-coated well and incubated for 30 min. The excess was rinsed away with PBS before imaging (Supplementary Fig. 3).

Probe density calibration

Lipid vesicles. Lipid vesicles were prepared with 100% 1,2-Dioleoyl-sn-glycero-3-phosphocholine (DOPC) or with 99.5% DOPC and 0.5% Texas Red DHPE (TR-DHPE). Lipid was dissolved in chloroform in a round-bottom flask and dried with a rotary evaporator and under an ultrahigh purity N_2 stream. The dried lipids were subsequently resuspended in Nanopure water at 2 mg ml^{-1} and endured three freeze–thaw cycles in acetone and dry-ice bath or 40 °C water bath. Lipids were then extruded ten times through a high-pressure extruder assembled with a 0.2 µm membrane to obtain uniform vesicles.

Supported lipid bilayer preparation. A glass-bottom 96-well plate was used for preparing supported lipid bilayers. Each well was filled and soaked with ethanol for 15 min and rinsed with 5 ml Nanopure water. Subsequently, 200 µl of 6 M NaOH solution was added to each well for base etching at room temperature for 1 h. After washing each well with 10 ml Nanopure water, lipid mixtures containing different percentage of TR-DHPE vesicles (0.01–0.5%) were added at 0.5 mg ml^{-1} in PBS to coat the glass surfaces for 20 min. After the lipid vesicles fused to the surfaces, the wells were rinsed with 10 ml water and 10 ml PBS and imaged with a fluorescence microscope to create a standard curve for probe density calibration.

Solution phase standard curve preparation. Surfaces were first washed with ethanol and water and passivated with 1% BSA to prevent any surface adsorption. Different concentrations of TR-DHPE

(2.96–740 nM) and a series of Cy3B-oligo solutions (10–500 nM) were then added to each well and their bulk fluorescence intensity in solution was measured with a fluorescence microscope (4 µm above surface) to create a standard curve (Supplementary Fig. 4).

Cell culture and transfection

NIH3T3 cells (ATCC, catalog no. CRL-1658) were cultured in Dulbecco's Modified Eagle Medium (DMEM) (10% cosmic calf serum, 1% penicillin–streptomycin (P/S)) at 37 °C with 5% CO_2. MEF and MEF vinculin null cells were obtained from the Garcia Laboratory at Georgia Institute of Technology and cultured in DMEM (10% fetal bovine serum, 1% P/S) at 37 °C with 5% CO_2. Cells were passaged at 80% confluency every 2 days by detaching using trypsin and replating at lower density. For MEF vinculin null cells, a plasmid encoding full-length vinculin and GFP was used for transfection. Cells were seeded in a six-well plate and transfected with 0, 0.25, 0.5, 2 or 3 µg of the plasmid for 24 h. The expression was validated by flow cytometry (Fig. 2i).

Mouse platelets

Blood of C57Bl/6J mice were collected after cardiac puncture or via retro-orbital plexus, and anticoagulated with acid-citrate-dextrose. After mixing with an equal volume of Tyrode's buffer (140 mM NaCl, 2.7 mM KCl, 0.4 mM NaH_2PO_4, 10 mM $NaHCO_3$, 5 mM dextrose, 10 mM HEPES, 3 U apyrase), mouse platelets were isolated by centrifugation at 200*g* for 5 min and subsequently supplemented with 1 U apyrase and 1 µM prostaglandin E1. Finally, the mouse platelets were spun down at 700*g* for 5 min and resuspended in Walsh buffer (137 mM NaCl, 2.7 mM KCl, 1 mM $MgCl_2$, 3.3 mM NaH_2PO_4, 20 mM HEPES, 0.1% glucose, 0.1% BSA, pH 7.4) at a density of ~1×10^9 platelets ml^{-1}.

Fluorescence microscopy

Integrin tension imaging. Imaging was conducted with a Nikon Ti2-E microscope. All the fibroblast cells were plated onto the DNA probe substrates in DMEM (10% serum, 1% P/S) and allowed to attach for 15–20 min in the incubator at 37 °C. Then, the cells were allowed to spread further at room temperature and imaged up until 60 min after plating in reflection interference contrast microscopy (RICM), Cy3B and Atto647N channels with accommodating filter settings and a sCMOS detector.

Mouse platelets were plated onto the DNA probe substrates in 1× Tyrode's buffer (134 mM NaCl, 12 mM $NaHCO_3$, 2.9 mM KCl, 0.34 mM NaH_2PO_4, 5 mM glucose, 5 mM HEPES, 0.1% BSA, pH 7.4) supplemented with 2 mM $CaCl_2$, 1 mM $MgCl_2$ and 10 µM ADP, and imaged at room temperature up until 60 min after plating in RICM, Cy3B and Atto647N channels.

Immunostaining. Cells incubated on DNA probe substrates were fixed in 4% formaldehyde for 10 min, followed by two gentle PBS washes and permeabilization with 0.1% Triton X-100 in PBS for 10 min. The cells were then blocked in 1% BSA for 1 h and then stained. Fixed cells were incubated with primary antibodies (anti-YAP: 2 µg ml^{-1}, anti-pFAK Y397: 5 µg ml^{-1} in 1% BSA) at 4 °C overnight. After rinsing three times with PBS, cells were incubated in secondary antibody (2 µg ml^{-1} in 1% BSA) for 1 h at room temperature. For actin straining, fixed cells were incubated with 0.5 µM SiR-actin or phalloidin iFluor 647 (1:1,000 dilution). Microscopy images were acquired with accommodating filter settings.

Flow cytometry

For all fibroblast cells, 1×10^4 cells were seeded on the TaCT substrate and collected by gentle scraping 60 min after seeding. After spinning down and washing in PBS containing 5 mM EDTA, the collected cells were resuspended in Dulbecco's phosphate-buffered saline (without Ca^{2+} and Mg^{2+}, with 5 mM EDTA) and immediately run through a flow cytometer for TaCT analysis.

For mouse platelets, 3 µl of the platelets were diluted in 600 µl of 1× Tyrode's buffer; 100 µl platelets were then added to the TaCT substrate with different supplements (Ca^{2+}, Mg^{2+}, ADP, Mn^{2+}). After 1 h, platelets were collected by pipetting them off from the substrate and then washed before running through flow cytometer for TaCT analysis.

Data analysis

Tension imaging data. All representative microscopy images were repeated collected and the results were confirmed from at least three independent replicates. All microscopy data were analyzed with Image J software.

For quantification of FRET efficiency, the Cy3B load-bearing strand and Atto647N peeling strand were annealed and immobilized on a biotin substrate and imaged to obtain the fluorescence intensity with both donor and acceptor present (I_{DA}). Similarly, Cy3B load-bearing strand and amine peeling strand were annealed and immobilized on a biotin substrate and imaged to obtain fluorescence intensity when only the donor was present (I_D). After sCMOS background subtraction of the images, the fluorescence intensity in Cy3B was averaged from five different positions of the substrates. The FRET efficiency was calculated with the equation $1 - I_{DA}/I_D$.

The probe density was estimated as described previously in literature[24]. Briefly, peeling probe and TGT substrates with unquenched Cy3B fluorescence strand were prepared. A calibration curve was prepared with fluorescent supported lipid bilayers to provide a count for molecules μm^{-2}, and the F-factor was calculated using a standard curve with a series of Cy3B concentrations (Supplementary Fig. 4). The average intensity of three substrates was used to calculate the probe density using the calibration curve.

Microscopy images of integrin tension were presented in formats including raw data, background subtracted or normalized molecular tension images, and %peel/percentage rupture (%rupture). For quantitative analysis of microscopy data with cells, the sCMOS background was subtracted, and the fluorescence intensity (mean ± s.d.) of the substrate background was used as a threshold. Raw integrated intensity, contact area and tension area of the regions of interest of the cells were measured and plotted. The tension signal in Cy3B for each image was used to calculate the %peel or %rupture according to literature (Supplementary Fig. 10)[24].

Flow cytometry data. Flow cytometry data were analyzed with Flowjo software. Briefly, the debris and aggregated cells were gated out by first identifying the live cells using the forward scatter and side scatter area, and then the singlet cells using the forward and side scatter height (Supplementary Fig. 11). Following gating, the fluorescence signal of each viable singlet cell in the Atto647N channel and Cy3B channel was measured and analyzed. The signal intensity was presented in histograms, and the median fluorescence intensity (MFI) or gMFI was used for comparison between groups. The percentage of positive cells was determined by creating a vertical gate in the histogram of the negative control group so that ~99.5% of cells in the negative control had a lower fluorescence than the gate. We anticipate that TaCT has a detection limit similar to that of any other flow cytometry assay.

Materials. All reagents and equipment used are listed in Supplementary Tables 3 and 4.

Reporting summary

Further information on research design is available in the Nature Portfolio Reporting Summary linked to this article.

Data availability

A data summary file containing all individual replicate data from the main text, all individual replicate data from the supporting information and all *P* values from statistical analyses performed in this manuscript is provided at https://osf.io/hkrve/?view_only=cc90b513cb5547358c652e5ace836106. Source data are provided with this paper.

Code availability

Code used for oxDNA data analysis and graph generation is publicly available online at https://github.com/SalaitaLab/Tension_activated_cell_tagging.

References

34. Engel, M. C. et al. Force-induced unravelling of DNA origami. *ACS Nano* **12**, 6734–6747 (2018).

Acknowledgements

K.S. acknowledges support from the National Institutes of Health through the National Institute of General Medical Sciences (NIGMS) grants RM1GM145394 and R01GM131099 and the National Institute of Allergy and Infectious Diseases grant no. AI172452.

Author contributions

R.M. and K.S. conceived the idea and wrote the manuscript. R.M., A.V., S.A.R. and B.R.D. carried out experiments and data analysis. A.V. performed oxDNA simulation. W.C., R.L. and B.P. provided mouse platelets. All authors contributed to editing the manuscript.

Competing interests

The authors declare no competing interests.

Additional information

Extended data is available for this paper at https://doi.org/10.1038/s41592-023-02030-7.

Supplementary information The online version contains supplementary material available at https://doi.org/10.1038/s41592-023-02030-7.

Correspondence and requests for materials should be addressed to Khalid Salaita.

Peer review information *Nature Methods* thanks the anonymous reviewers for their contribution to the peer review of this work. Peer reviewer reports are available. Primary Handling Editor: Madhura Mukhopadhyay, in collaboration with the *Nature Methods* team.

https://doi.org/10.1038/s41592-023-02030-7

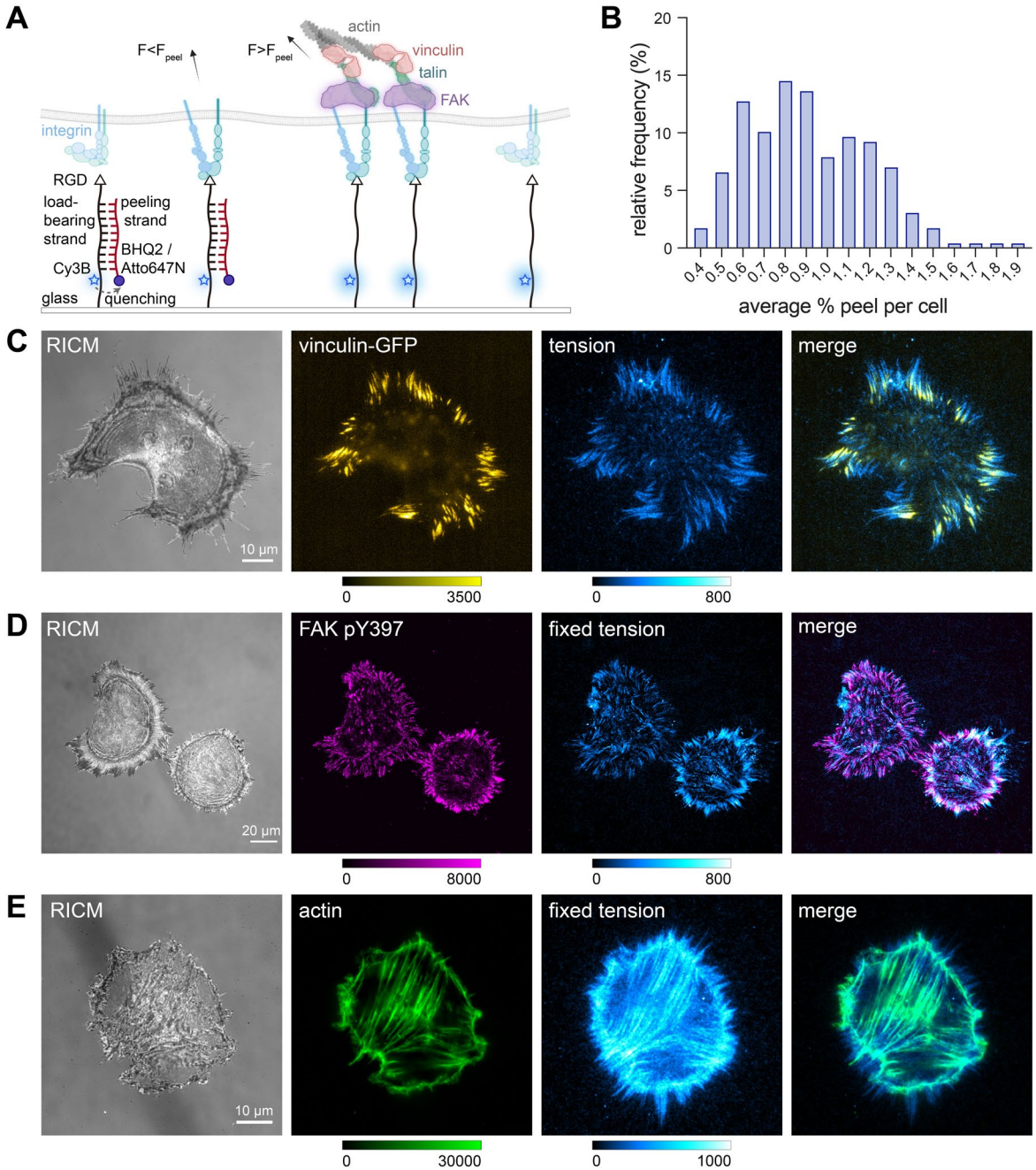

Extended Data Fig. 1 | Mapping integrin forces with peeling probe. (**a**) Scheme showing that when integrin is in the inactive state, the peeling probe remains in the duplex form. As integrin binds and pulls on the RGD ligand, if $F < F_{peel}$, the peeling strand is intact, and if $F > F_{peel}$, the duplex dehybridizes and the Cy3B fluorescence turns on. FA proteins such as vinculin, talin, and FAK, as well as actin cytoskeleton participate extensively during the integrin force generation and mechanotransduction. (**b**) Histogram of 227 NIH3T3 cells showing the distribution of average %peel/µm^2 per cell after 1 h incubation on peeling probe substrate. Data acquired from 3 biological replicates, bin width = 0.1%. (**c**) Representative microscopy images show that GFP-vinculin colocalized with integrin tension signal. Images were acquired with MEF GFP-vinculin cells that were cultured on peeling probe substrate (n = 3). (**d**) Representative microscopy images show that the phosphorylated FAK (pY397) colocalized with fixed integrin tension signal. MEF cells were incubated on peeling probe substrate for 40–45min, fixed and stained with Rabbit anti-FAK pY397 and Alexa488 labeled secondary antibody, followed by imaging (n = 3). (**e**) Representative microscopy images show that the actin stress fibers colocalized with fixed tension signal (n = 3). MEF cells were incubated on peeling probe substrate for 60–90 min, fixed and stained with Alexa647-phalloidin, followed by imaging.

https://doi.org/10.1038/s41592-023-02030-7

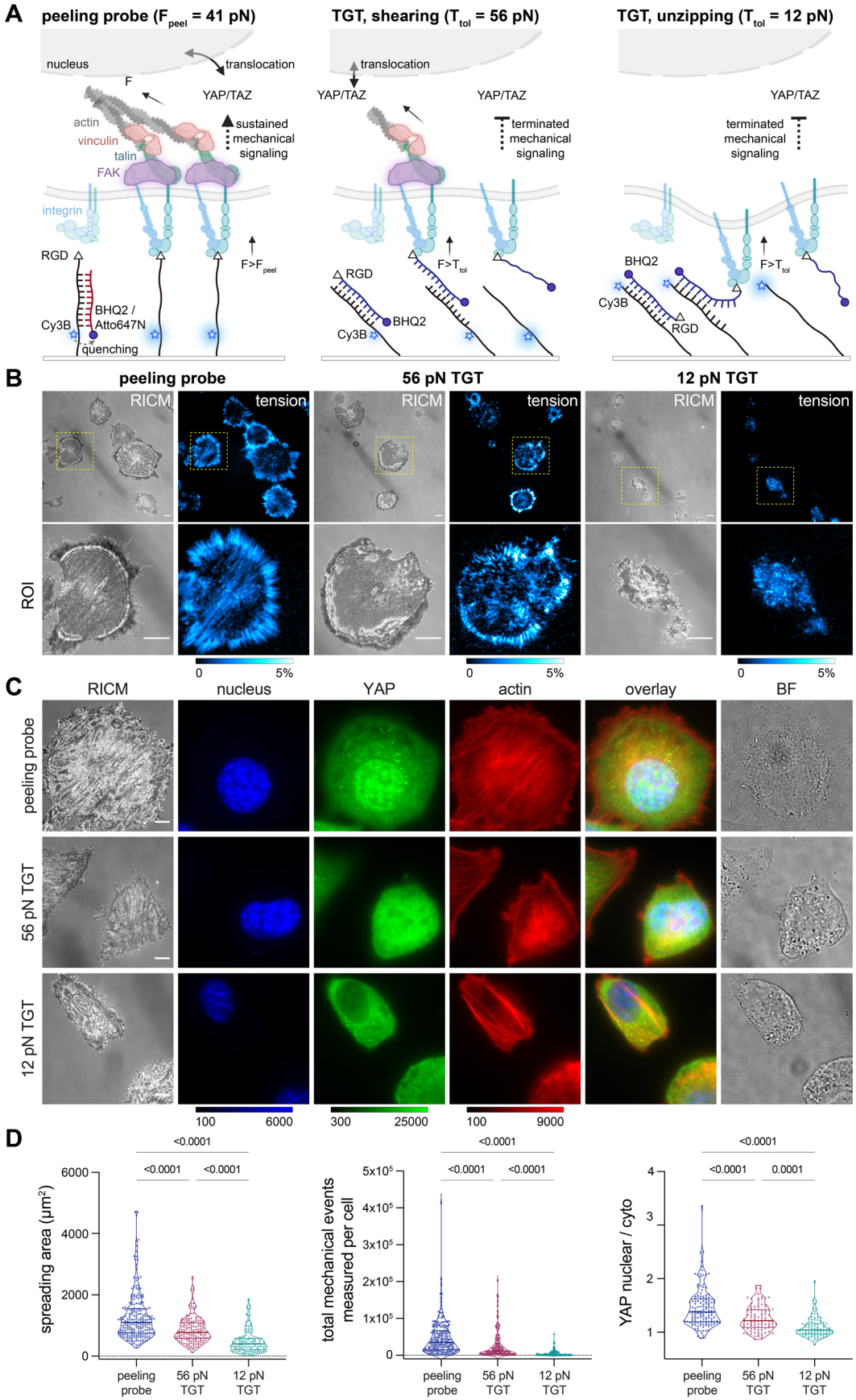

Extended Data Fig. 2 | See next page for caption.

https://doi.org/10.1038/s41592-023-02030-7

Extended Data Fig. 2 | Peeling probe does not perturbate mechanotransduction unlike TGTs. (**a**) Schematics comparing the mechanism of TaCT/peeling probe and TGTs. Peeling probe maps integrin tension greater than 41 pN as the BHQ2 strand is separated, and the RGD anchor remains despite the duplex dehybridization. In contrast, TGTs map integrin forces greater than 56 or 12 pN in the shearing or unzipping geometry. The force-induced rupture of the duplex generates a Cy3B turn-on fluorescence signal as the top BHQ2 strand separates from the Cy3B anchor strand. Unlike peeling strand, the loss of the RGD anchors in TGTs terminates mechanotransduction through integrins. (**b**) Representative microcopy images of NIH3T3 cells incubated on peeling probe or TGT substrates for ~45–60 min (n = 3). Second row of images show the zoom-in view of the ROIs marked with the yellow dashed box. Intensity bar for Cy3B image indicates the peeling/rupturing percentage of the probes. Scale bar = 10 µm. (**c**) Microscopy images of NIH3T3 cells incubated on peeling probe or TGT substrates for ~90 min, fixed and stained for nucleus (DAPI), actin (SirActin), and YAP (Alexa488 conjugated antibody). Scale bar = 5 µm. Intensity bar indicates the gray value. (**d**) Quantitative analysis of the spreading area, %peel or %rupture, and YAP translocation for NIH3T3 cells incubated on three substrates for 60 min. For spreading area and tension quantification, data was collected from 3 biological replicates (n = 227, 150, and 105 for cells on peeling probe, 56 pN TGT, and 12 pN TGT substrate). For analysis on YAP translocation, images in DAPI channel were used as masks to quantify the mean fluorescence intensity of nuclear YAP and cytoplasm YAP. Data was acquired from 3 biological replicates (total n = 134, 98, and 86 cells for peeling probe, 56 pN TGT, and 12 pN TGT substrate). Plots show lines at the median and interquartile values. Statistical analysis was performed with one-way ANOVA and Tukey's multiple comparison test.

https://doi.org/10.1038/s41592-023-02030-7

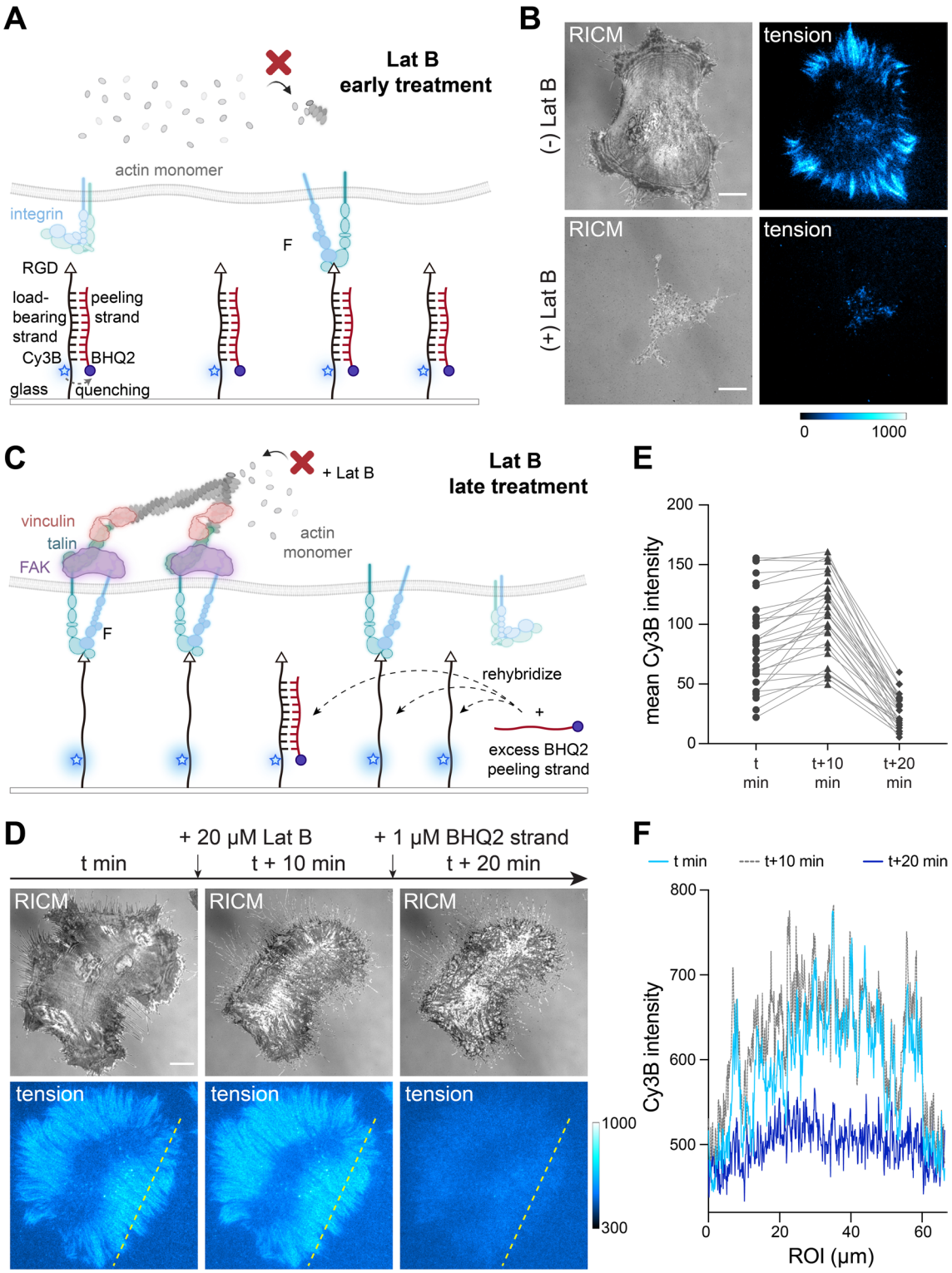

Extended Data Fig. 3 | Lat B inhibition of cells. (**a**) Scheme showing that Lat B early treatment inhibits integrin force generation by inhibiting actin polymerization. (**b**) Representative RICM and Cy3B microscopy images of MEF cells incubated on peeling probe substrate after early Lat B treatment. Cells were treated with 20 μM Lat B after 15 min of plating on the substrate and imaged after 45 min of incubation. Scale bar = 10 μm. (**c**) Scheme showing that when integrin force signals are already generated on peeling probe substrate, if the force transmission is terminated by late Lat B treatment, with additional BHQ2 peeling strand the peeling probe can rehybridize to the duplex form. (**d**) Representative RICM and raw Cy3B microscopy images of MEF cells treated with 20 μM Lat B 50 min after seeding. The tension signal remained after 10 min of Lat B treatment and diminished after the addition of excess BHQ2 peeling strand. Scale bar = 5 μm. (**e**) Quantitative analysis of tension signal changes after Lat B treatment and the addition of BHQ2 peeling strand in n = 30 cells. (**f**) Linescan of the ROI (yellow dashed line) in (D) before Lat B treatment, with Lat B treatment, and with excess BHQ2 peeling strand.

https://doi.org/10.1038/s41592-023-02030-7

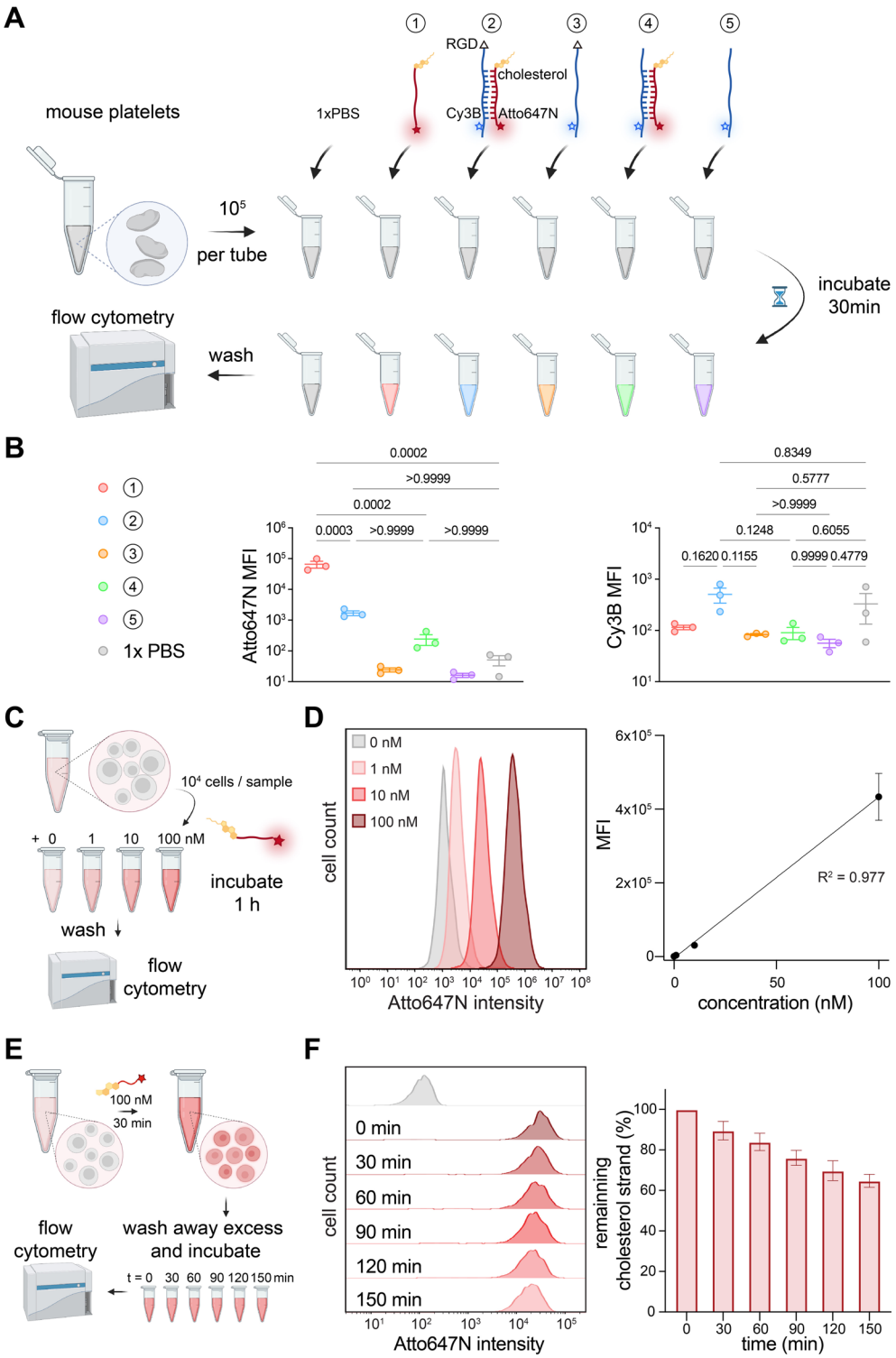

Extended Data Fig. 4 | Cholesterol DNA strands association and dissociation in cells. (**a**) Scheme showing flow cytometry measurements of the DNA strands uptake in solution. Mouse platelets were incubated with 50 nM of cholesterol peeling strand, TaCT duplex, load-bearing strand, TaCT duplex lacking RGD, and load-bearing strand lacking RGD in Tyrode's buffer for 30 min and spun down three times to wash away the excess oligos. The association was measured in both Atto647N and Cy3B channels by a flow cytometer. (**b**) Cy3B and Atto647N median fluorescence intensity (MFI) of platelets incubated with different oligonucleotides. Data collected from 3 replicates (mean ± SEM). Statistical analysis was performed by one-way ANOVA and Tukey's multiple comparison. (**c**) Scheme showing flow cytometry measurements of the concentration dependent incorporation of cholesterol peeling strand. MEF cells were incubated with 0, 1, 10, and 100 nM of cholesterol peeling strand for 1 h. The excess cholesterol peeling strand was washed away by spinning down in PBS three times, and the fluorescence intensity of cells was measured by a flow cytometer. (**d**) Representative histogram of cholesterol peeling strand association in cells. Atto647N MFI was plotted from 3 replicates (mean ± SD). Linear relationship between cholesterol strand concentration and cell association was found, $R^2 = 0.977$. (**e**) Scheme showing the measurement of cholesterol peeling strand dissociation from the cell. NIH3T3 cells were incubated with 100 nM cholesterol peeling strand for 30 min and rinsed with PBS 3 times. Cells were divided into 6 aliquots and the remaining cholesterol strand in cells was measured every 30 min for 150 min by flow cytometry. (**f**) Representative histogram shows the decay of fluorescence in cells over time. The normalized MFI from 2 replicates was plotted to show the dissociation of cholesterol strand over time in NIH3T3 cells (mean ± SD).

https://doi.org/10.1038/s41592-023-02030-7

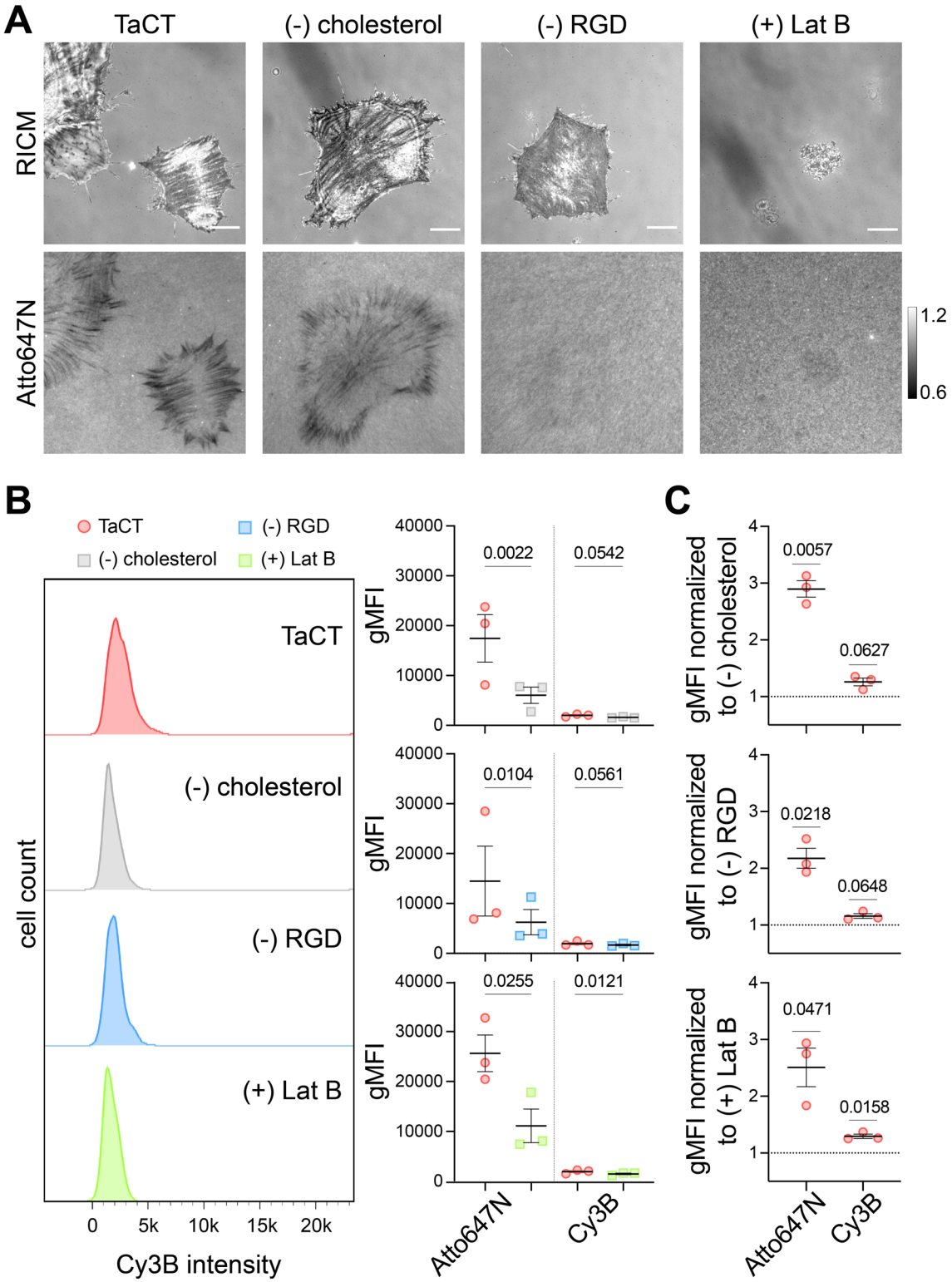

Extended Data Fig. 5 | Control experiments supporting the concept of TaCT. (**a**) Representative microscopy images of NIH3T3 cells cultured on TaCT substrate, or control substrate lacking cholesterol, lacking RGD, or treated with Lat B (n = 3). Atto647N shows the signal normalized to the background intact probes. Scale bar = 10 µm. (**b**) Representative flow cytometry histograms show that NIH3T3 cells in TaCT, (−)cholesterol, (−)RGD, and (+)Lat B groups had indistinguishable Cy3B intensity. Quantitative analysis (mean ± SEM) shows that cells cultured on TaCT substrate had similar level of geometric mean fluorescence intensity (gMFI) compared to control groups in Cy3B channel, despite higher Atto647N gMFI. Data collected from 3 replicates for each control, and statistical analysis was performed using ratio paired two-tailed Student's t-test. (**c**) Plots show the gMFI of cells after TaCT normalized to different controls in both Atto647N and Cy3B channels (n = 3, mean ± SEM). One sample t-test (two-tailed) was used for statistical analysis to test whether TaCT signal is significantly different in Atto647N and Cy3B compared to a hypothetical value of 1 (representing no TaCT signal in the corresponding control group). TaCT signal in Atto647N channel consistently provides 2 to 3 fold higher gMFI.

https://doi.org/10.1038/s41592-023-02030-7

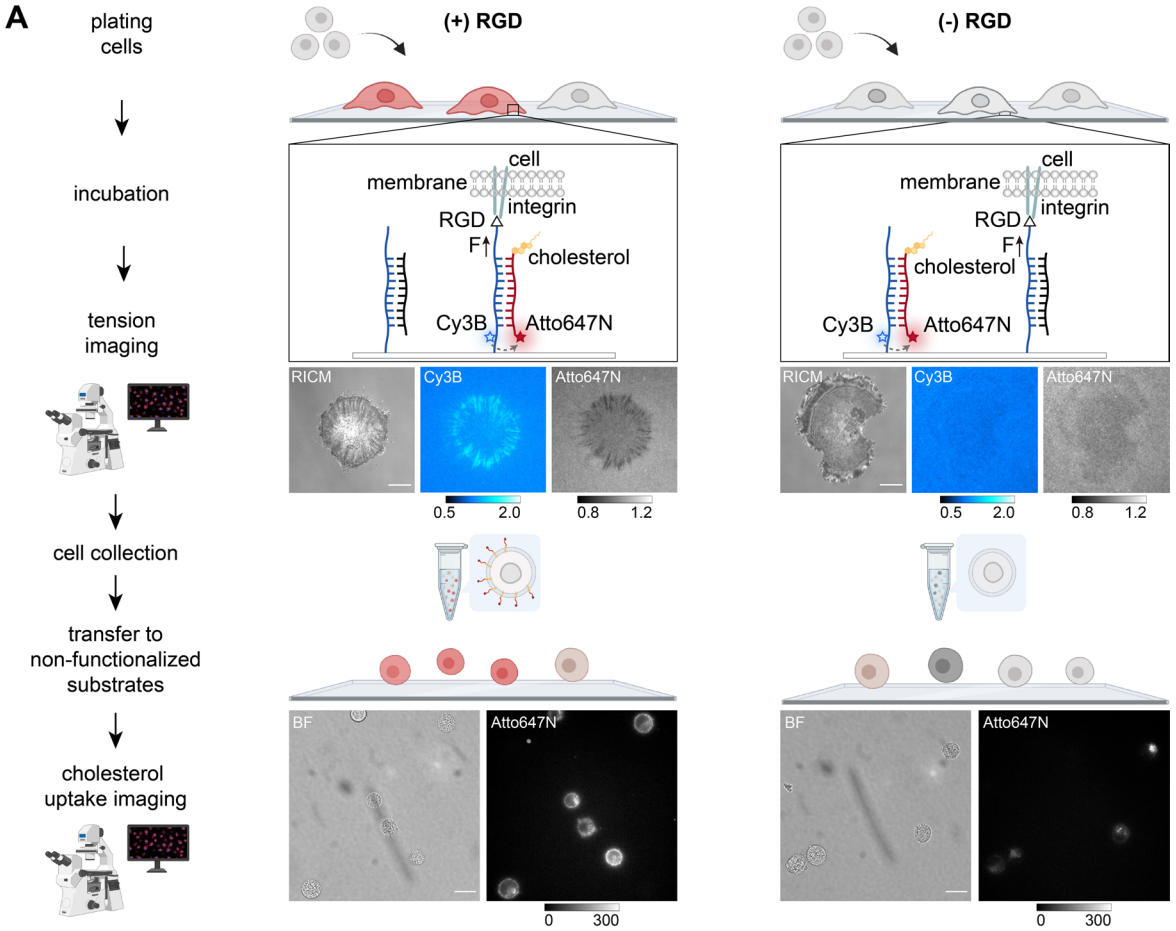

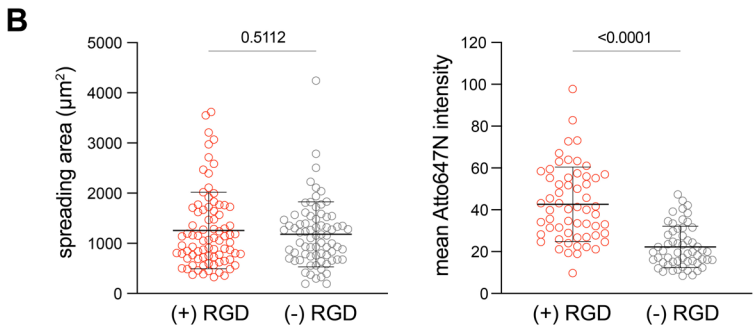

Extended Data Fig. 6 | Spreading control for TaCT. (**a**) Scheme and representative microscopy data showing that TaCT signal is not due to spreading of the cells on the substrate. NIH3T3 cells were incubated on a TaCT substrate doped with a non-fluorescent DNA duplex, or a TaCT substrate lacking RGD doped with a non-fluorescent DNA duplex presenting the RGD motif, and imaged 45 min–60 min after seeding. After confirming the cell spreading, cells were collected, rinsed, and added to non-fluorescent glass substrate to image the cholesterol peeling strand incorporation in the cells. Tension images were normalized to the background of intact probes. Scale bar = 10 μm. (**b**) Quantitative analysis of the cell spreading area (n = 82 and 74 cells) and cholesterol peeling strand incorporation (n = 58 and 56 cells) for cells incubated on TaCT (+)RGD or (−)RGD substrates. Data was collected from three replicates and statistical analysis was performed using two-tailed Student's t-test.

https://doi.org/10.1038/s41592-023-02030-7

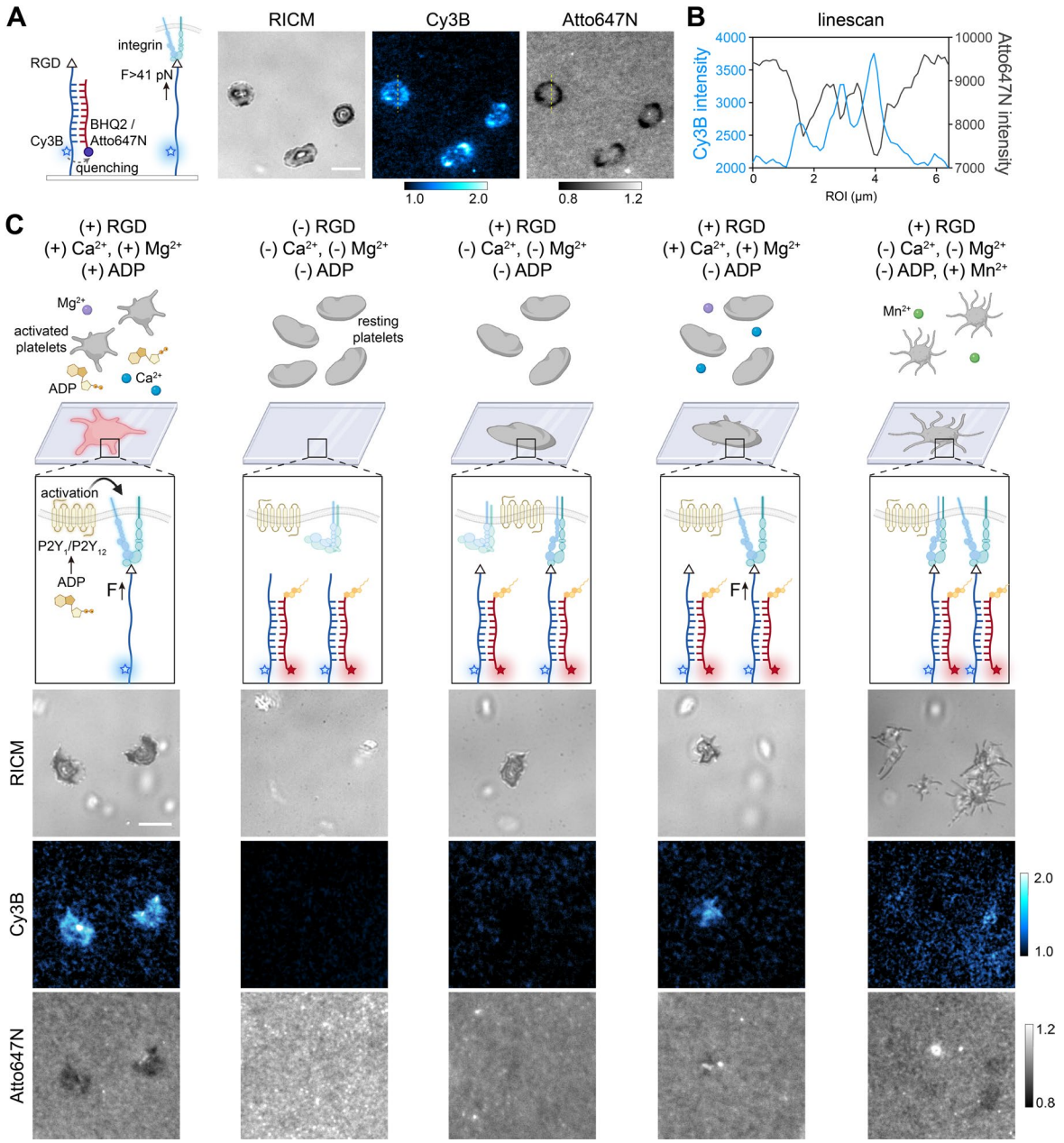

Extended Data Fig. 7 | TaCT in Platelets. (**a**) Scheme and representative microscopy images showing tension mapping with peeling probe in mouse platelets (n = 3). Tension images were normalized to the background of intact peeling probes, scale bar = 5 µm. (**b**) Linescan of the ROI (yellow dashed line) shows anti-colocalization of Cy3B and Atto647N intensities from raw data. (**c**) Scheme and representative images show mouse platelets incubated on the TaCT substrate in different buffer conditions (n = 3). RGD, Ca^{2+}, Mg^{2+}, and ADP leads to platelets activation, and withholding any of them results in no/impaired activation. Tension images were normalized to the background of intact TaCT probes, scale bar = 5 µm.

nature research

Corresponding author(s): Khalid Salaita

Last updated by author(s): May 30, 2022

Reporting Summary

Nature Research wishes to improve the reproducibility of the work that we publish. This form provides structure for consistency and transparency in reporting. For further information on Nature Research policies, see our Editorial Policies and the Editorial Policy Checklist.

Statistics

For all statistical analyses, confirm that the following items are present in the figure legend, table legend, main text, or Methods section.

n/a	Confirmed	
☐	☒	The exact sample size (*n*) for each experimental group/condition, given as a discrete number and unit of measurement
☐	☒	A statement on whether measurements were taken from distinct samples or whether the same sample was measured repeatedly
☐	☒	The statistical test(s) used AND whether they are one- or two-sided *Only common tests should be described solely by name; describe more complex techniques in the Methods section.*
☐	☒	A description of all covariates tested
☐	☒	A description of any assumptions or corrections, such as tests of normality and adjustment for multiple comparisons
☐	☒	A full description of the statistical parameters including central tendency (e.g. means) or other basic estimates (e.g. regression coefficient) AND variation (e.g. standard deviation) or associated estimates of uncertainty (e.g. confidence intervals)
☐	☒	For null hypothesis testing, the test statistic (e.g. *F*, *t*, *r*) with confidence intervals, effect sizes, degrees of freedom and *P* value noted *Give P values as exact values whenever suitable.*
☒	☐	For Bayesian analysis, information on the choice of priors and Markov chain Monte Carlo settings
☒	☐	For hierarchical and complex designs, identification of the appropriate level for tests and full reporting of outcomes
☒	☐	Estimates of effect sizes (e.g. Cohen's *d*, Pearson's *r*), indicating how they were calculated

Our web collection on statistics for biologists contains articles on many of the points above.

Software and code

Policy information about availability of computer code

Data collection	NIS-Elements software was used for microscopy data collection. CytExpert 2.3 was used for flow cytometry data collection. OpenLAB CDS ChemStation edition from Agilent Technologies was used for HPLC data collection. Simulation data is collected with code at https://github.com/SalaitaLab/Tension_activated_cell_tagging.
Data analysis	Fiji ImageJ (2.9) was used for microscopy data analysis. Flowjo was used for flow cytometry data analysis. Graphpad Prism 9 was used to make plots and perform statistical analysis.

For manuscripts utilizing custom algorithms or software that are central to the research but not yet described in published literature, software must be made available to editors and reviewers. We strongly encourage code deposition in a community repository (e.g. GitHub). See the Nature Research guidelines for submitting code & software for further information.

Data

Policy information about availability of data

All manuscripts must include a data availability statement. This statement should provide the following information, where applicable:

- Accession codes, unique identifiers, or web links for publicly available datasets
- A list of figures that have associated raw data
- A description of any restrictions on data availability

Excel Data summary file containing all individual replicate data from main text, all individual replicate data from supporting information, and all p values from statistical analyses performed are provided in this manuscript at https://osf.io/hkrve/?view_only=cc90b513cb5547358c652e5ace836106.

Field-specific reporting

Please select the one below that is the best fit for your research. If you are not sure, read the appropriate sections before making your selection.

☒ Life sciences ☐ Behavioural & social sciences ☐ Ecological, evolutionary & environmental sciences

For a reference copy of the document with all sections, see nature.com/documents/nr-reporting-summary-flat.pdf

Life sciences study design

All studies must disclose on these points even when the disclosure is negative.

Sample size	All experiments were performed with multiple cells in each condition. For microscopy, each group in every experiment has at least ~20 cells imaged, and for flow cytometry, each group in every experiment has 10000 cells seeded to substrate. For a few experiments that the cells were not completely collected after treatment, there were at least >2000 cells collected. This sample size is sufficient to represent the experiment results.
Data exclusions	No data was excluded from the described results.
Replication	All experimental findings were based on at least 3 distinct replicates, except for the experiment using 3T3 cells in the Extended Figure 4F which was based on 2 replicates. For this experiment, we have observed a similar trend in mouse platelets with 3 replicates (Figure S6B). Therefore, we did not pursue a third replicate in 3T3 cells as the cholesterol dissociation from cell membrane is already illustrated. The relative trends between groups for each set of all experiments were consistent.
Randomization	We did not randomize samples because randomization is not necessary to investigate the parameters or perform the techniques described in this study. Individual experiments were grouped for statistical analysis.
Blinding	No group allocation was performed, therefore no blinding to group assignment was required.

Reporting for specific materials, systems and methods

We require information from authors about some types of materials, experimental systems and methods used in many studies. Here, indicate whether each material, system or method listed is relevant to your study. If you are not sure if a list item applies to your research, read the appropriate section before selecting a response.

Materials & experimental systems

n/a	Involved in the study
☐	☒ Antibodies
☐	☒ Eukaryotic cell lines
☒	☐ Palaeontology and archaeology
☐	☒ Animals and other organisms
☒	☐ Human research participants
☒	☐ Clinical data
☒	☐ Dual use research of concern

Methods

n/a	Involved in the study
☒	☐ ChIP-seq
☐	☒ Flow cytometry
☒	☐ MRI-based neuroimaging

Antibodies

Antibodies used	Recombinant Anti-FAK (phospho Y397) antibody (Abcam, ab81298, LOT GR327575778-6); Anti-YAP1 Antibody (63.7, Santa Cruz, sc-101199); Anti-rabbit IgG (H+L), F(ab')2 Fragment, Alexa488 (Cell signaling, 4412, LOT:23); Anti-mouse IgG H&L, Alexa488 (Abcam, ab150113, LOT GR3225138-1)
Validation	Antibodies are all validated by the manufacturers according to the product documentation.

Eukaryotic cell lines

Policy information about cell lines

Cell line source(s)	Mouse embryonic fibroblast cells (wild type and vinculin null) were gifted from the lab of Prof. Andres Garcia. NIH3T3 cells were obtained from ATCC.
Authentication	The cell lines have not been authenticated.
Mycoplasma contamination	The Mouse embryonic fibroblast cells (wild type and vinculin null) were not tested for mycoplasma contamination. No mycoplasma was detected in NIH3T3 cells according to ATCC quality control documentation.

Commonly misidentified lines (See ICLAC register)	NA

Animals and other organisms

Policy information about studies involving animals; ARRIVE guidelines recommended for reporting animal research

Laboratory animals	Mouse platelets were provided by Renhao Li and Brian Petrich lab at Emory.
Wild animals	NA
Field-collected samples	NA
Ethics oversight	IACUC oversees the animal facility at Emory.

Note that full information on the approval of the study protocol must also be provided in the manuscript.

Flow Cytometry

Plots

Confirm that:

☒ The axis labels state the marker and fluorochrome used (e.g. CD4-FITC).

☒ The axis scales are clearly visible. Include numbers along axes only for bottom left plot of group (a 'group' is an analysis of identical markers).

☒ All plots are contour plots with outliers or pseudocolor plots.

☒ A numerical value for number of cells or percentage (with statistics) is provided.

Methodology

Sample preparation	Cells were collected after experiment procedures and loaded into the flow cytometer. See Methods section for details on experiment procedures.
Instrument	CytoFLEX V0-B3-R1 equipped with a 488 nm and 638 nm laser.
Software	Data collection: CytExpert 2.3 Data analysis: Flowjo V10 and Prism 9.
Cell population abundance	Median or geometric mean fluorescence intensity was calculated from each sample containing 10000 cells before any gating.
Gating strategy	For each sample, all events were shown on a forward scatter area vs side scatter area plot and a "viable singlets" gate is draw to approximately include this population. The events within the gate is then shown in a dot plot with axis of Atto647N/Cy3B/ CMFDA intensity. See figure S9.

☒ Tick this box to confirm that a figure exemplifying the gating strategy is provided in the Supplementary Information.